Stellar Populations and Mass-Loss in M15: A *Spitzer* Detection of Dust in the Intra-Cluster Medium

Martha L. Boyer[1,2], Charles E. Woodward[2], Jacco Th. van Loon[3], Karl D. Gordon[4], A. Evans[3], Robert D. Gehrz[2], L. Andrew Helton[2], Elisha F. Polomski[2]

ABSTRACT

We present *Spitzer Space Telescope* IRAC and MIPS observations of the galactic globular cluster M15 (NGC 7078), one of the most metal-poor clusters with a [Fe/H] = -2.4. Our *Spitzer* images reveal a population of dusty red giants near the cluster center, a previously detected planetary nebula (PN) designated K648, and a possible detection of the intra-cluster medium (ICM) arising from mass loss episodes from the evolved stellar population. Our analysis suggests $(9 \pm 2) \times 10^{-4}$ $M_{\odot}$ of dust is present in the core of M15, and this material has accumulated over a period of $\approx 10^6$ yrs, a timescale ten times shorter than the last galactic plane crossing event. We also present *Spitzer* IRS follow up observations of K648, including the detection of the [Ne II] λ12.81 μm line, and discuss abundances derived from infrared fine structure lines.

Subject headings: globular clusters: individual (M15)—ISM: evolution—stars: AGB and post-AGB—stars: mass loss—planetary nebulae: individual (K648)

1. INTRODUCTION

Mass loss in evolved stellar populations affects the chemical evolution of the interstellar medium (ISM) and mass loss from individual stars governs post main sequence evolution. The amount and duration of mass loss that occurs in giant stars remains one of the most uncertain parameters in stellar evolution theory and the effect of these processes on the

[1]mboyer@astro.umn.edu

[2]Astronomy Department, School of Physics and Astronomy, 116 Church Street, S.E., University of Minnesota, Minneapolis, MN 55455

[3]Astrophysics Group, School of Physical & Geographical Sciences, Keele University, Staffordshire ST5 5BG, UK

[4]Steward Observatory, University of Arizona, 933 North Cherry Avenue, Tucson, AZ 85721

inferences derived from stellar population models can be significant. Given the wide use of these models (e.g., in inferring stellar masses of high-redshift galaxies), understanding the mass losing process is vital for a range of problems in astrophysics. Although dust constitutes a small fraction of the total mass lost, it is frequently used as a marker as it is optically thin and its thermal emission is readily detectable in a variety of environments.

Globular clusters (GCs), believed to have formed during the assemblage of the Galaxy, are coeval samples of stars at common, well-determined distances with nearly uniform initial compositions. GCs enable study of the chemical enrichment of the interstellar medium arising from mass ejection during the post-main sequence evolution of stars. Red Giant stars, especially those ascending the Asymptotic Giant Branch, are expected to develop winds that inject processed material into the intra-cluster medium (ICM) during post-main sequence evolution. These winds contain gas and solid phase materials, the latter in the form of dust grains that condense from the metals. However, detection of thermal emission arising from intra-cluster medium dust has been elusive, suggesting that the ICM in GCs is 100 to 1000 times less massive than expected from current stellar evolution theory and observations of mass-losing stars in clusters and in the solar neighborhood.

The circumstellar environments of stars in the late stages of evolution, when most mass loss occurs, are most effectively detected and studied in the infrared (IR). IR surveys conducted by *IRAS*, *2MASS,* and *ISO* revealed populations of dust-enshrouded asymptotic giant branch (AGB) and red supergiant (RSG) stars in the Galactic bulge (van Loon et al. 2003), the Large Magellanic Cloud (LMC) (Zijlstra et al. 1996; van Loon et al. 1997; Trams et al. 1999), and in galactic Globular Clusters (Ramdani & Jorissen 2001; Origlia et al. 2002). GCs are expected to contain dust from episodes of mass loss in red giant branch (RGB) and AGB stars. The IR excess of their circumstellar dust emission is expected to peak between 20 μm to 30 μm, and thus photometry at wavelengths larger than 20 μm is necessary to estimate accurate dust masses lost by such stars. The amount of dust present in the intra-cluster medium (ICM) will vary depending on the cluster escape velocity, the time since last crossing of the Galactic disk where the ICM can be stripped away by the ISM, and the number of mass-losing stars. In general the dust in the ICM of GCs is expected to be $\simeq 10^{-2}$ to 10^{-3} $M_\odot$ for most galactic clusters. Globular clusters have reasonably homogeneous (in age and metallicity), well-understood stellar populations, so observations of ICM dust are reasonably straightforward to interpret to yield mass loss rates and duty cycles.

Previous attempts to detect the ICM in GCs suggest that the ICM density is well below that expected from predictions of the mass loss input from RGB and AGB stars, even considering the low metallicity of GCs. The lowest 3-σ upper limits to the ICM mass for 70 K dust are $\sim 6 \times 10^{-5}$ $M_\odot$ (Hopwood et al. 1999). Detecting thermal emission from the elusive

ICM in GCs is observationally challenging. Origlia et al. (2002) reported *ISO* observations of the IR thermal emission from the winds of individual RGB stars in six massive GCs (47 Tuc, NGC 362, Omega Cen, NGC 6388, M15, and M54) showing that, in those systems, stellar winds from these stars are enriching the ICM. Though thermal emission from the ICM material might be expected to be detectable, many attempts to do so with IR and millimeter observatories have produced only a single secure detection of ICM dust, a tentative (3.5-σ) detection of thermal emission in the core of the metal-poor GC M15 (Evans et al. 2003). Overall this result suggests that the ICM dust in GCs is significantly less massive than expected from current stellar evolution theory and observations of mass losing stars in GCs and the solar neighborhood.

The causes of the paucity of ICM emission have been proposed to be ram-pressure stripping of ICM gas during Galactic plane passage, blowout by nova explosions, fast winds from the stars themselves, radiative ejection by the sheer luminosity of cluster stars, and continuous ram-pressure from hot gas in the galactic halo. However, the dominant state of the ICM is unclear. Sensitive searches for neutral H in the ICM at radio wavelengths have yielded upper limits ≤ 0.1 $M_\odot$ (Birkinshaw et al. 1983), with a possible detection of ≈ 200 $M_\odot$ in NGC 2808 (Faulkner et al. 1991) and a 5σ detection of 0.3 $M_\odot$ in M15 (van Loon et al. 2006). Perhaps much of the ICM is ionized, as suggested by the high electron densities measured from pulsar timing in 47 Tuc (Freire et al. 2001). However, Hα searches have as yet been unsuccessful.

ICM dust grains in radiative thermal equilibrium should attain temperatures of 50 K to 80 K because of the high energy density of starlight within a GC (Forte et al. 2002) and thus be detectable as an IR excess (above the photospheric emission) in GCs at mid- to far-IR wavelengths. Here we present observations of the galactic GC M15 with the *Spitzer Space Telescope* (Werner et al. 2004), whose instrumental sensitivity enables detection of dust masses as low as 4×10^{-9} $M_\odot$ (assuming a population of grains radiating in thermal equilibrium, with integration times down to the background confusion limit) and therefore permits an unequalled opportunity to search for and set stringent limits on the "missing" ICM.

1.1. M15

M15 (NGC 7078), with [Fe/H] = -2.4 (Sneden et al. 1997), is one of the most metal poor GCs. It is a well-studied cluster, as it is home to the first planetary nebula (PN) discovered in a GC (K648, also designated as Ps-1, Pease (1928); Howard et al. (1997); Alves et al. (2000)) and to the first GC Low-Mass X-ray Binary source (X2127+119, Auriére

et al. (1984); Charles et al. (1986)). At least eight millisecond pulsars are also associated with the cluster (Kulkarni & Anderson 1996). M15 is generally believed to be a core-collapse GC, with a small, dense core containing approximately 4000 $M_\odot$ (Phinney 1996).

Properties of M15, reproduced from Hopwood et al. (1999), are listed in Table 1. Updated values as listed by Evans et al. (2003) include the escape velocity V_{esc} from Webbink (1985), and the time τ_c since the last plane crossing from Odenkirchen et al. (1997). The reddening and the distance are updated from Schlegel et al. (1998) and McNamara et al. (2004), respectively. Galactic coordinates for M15 are $l = 65.01°$ and $b = -27.31°$, placing the cluster ~ 4.5 kpc south of the galactic plane.

The total dust mass expected in a GC can be estimated using the following equation:

$$M_{dust} = \frac{\tau_c}{\tau_{HB}}\ N_{HB}\ \delta M\ \frac{10^{[Fe/H]}}{100}, \tag{1}$$

where τ_{HB} is the Horizontal Branch (HB) lifetime, N_{HB} is the number of HB stars, [Fe/H] is the cluster metallicity, and δM is the dust mass lost from each star at the tip of the RGB. The factor of 100 is the solar gas-to-dust ratio, which is scaled for the metallicity of M15 by adding the [Fe/H] factor. Using values typical of population II stars and this relationship, the expected dust mass in M15 has been estimated to be 3.7×10^{-3} $M_\odot$ by Evans et al. (2003) and 2.0×10^{-3} $M_\odot$ by Hopwood et al. (1999).

M15 is also home to the PN K648. K648 was the first globular cluster PN discovered, and subsequently it has been extensively studied at UV, optical and IR wavelengths to determine the chemical composition of the ejecta nebula and parameters of the central star (Barker et al. 1983; Adams et al. 1984; Howard et al. 1997; Bianchi et al. 2001; Dinerstein et al. 2003; Garnett & Lacy 1993). The study of post-AGB stellar evolution in old metal-poor, low-mass stars in GCs or the galactic halo can be greatly enhanced if the by-products of stellar nucleosynthesis can be measured. Enriched material produced in the RGB and AGB stages of stellar evolution are dispersed into outer layers of the stellar system and subsequent mass loss processes lead to the formation of a PN. Few PNe in the galactic halo population have been identified and only four of these PNe, including K648, BB-1, DdDM 1, and H4-1 are associated with globular clusters (Jacoby et al. 1997). Below, we present findings derived from a 5-15 μm IR spectrum of K648.

2. OBSERVATIONS

Image observations of the GC M15 were obtained on 2004 October 29 UT with the Multiband Imaging Photometer for *Spitzer* (MIPS) (Rieke et al. 2004) camera through the 24 μm and 70 μm filters and with the Infrared Array Camera (IRAC) (Fazio et al. 2004) at 3.6, 4.5, 5.8, and 8 μm conducted as part of the Gehrz Guaranteed Time Observing Program (GGTOP, PID 124). Raw data were processed with the *Spitzer* Science Center (SSC) pipeline version S11.4.0. To avoid saturation in IRAC, High Dynamic Range (HDR) mode was implemented, using 0.4 s, 10.4 s, and 98.6 s exposures. For each IRAC channel, 55 frames at seven dither positions were obtained with each HDR exposure time. With the MIPS camera, 596 dithered frames were taken at 24 μm along with 256 dithered frames at 70 μm.

Spitzer IRS spectra of the PN and other red sources detected in the IRAC images have been obtained as part of a follow on program using GGTOP time and these data are discussed below. Table 2 summarizes the observations discussed in this paper.

2.1. IRAC

The IRAC Basic Calibrated Data (BCD) images were post-processed to correct for various instrumental artifacts and were mosaicked using the 2005 May 09 version of the SSC Legacy MOPEX software (Makovoz & Marleau 2005). The MOPEX cosmetic correction was used to eliminate mux-bleed and column pull-down as described by the IRAC Data Handbook, v3.0.[1] The background matching correction was used to minimize pixel differences in overlapping areas of the mosaics. The MOPEX mosaicker also eliminated cosmic rays and other outliers in the data. The final IRAC mosaics are not subsampled, thus the pixel size of each final tiled image is 1.22″ per pixel covering an area $\sim$ 50 square arcminutes around the core (RA[J2000] = $21^{\rm h}$:$29^{\rm m}$:58″.38; Dec[J2000] = +12°:10′:00″.6) of M15 plus an off-field region of the same size 7′ to the north or south. A three color image combining 3.6 μm, 4.5 μm and 8 μm is presented in Fig. 1a. The diffuse ICM is not detected in the IRAC mosaics, even at 8 μm. However, the planetary nebula (K648) and several other dusty stellar objects become quite prominent at 8 μm.

Point source photometry was conducted using several stellar extraction routines including GlimpsePhot[2], DAOphot (Stetson 1987), and the astronomical point source extraction

[1]http://ssc.spitzer.caltech.edu/irac/dh/iracdatahandbook3.0.pdf

[2]http://www.astro.wisc.edu/sirtf/

(APEX) tool contained in the SSC MOPEX package. Severe stellar crowding towards the cluster core in the IRAC bands made reliable point-response-function (PRF) photometry challenging. The best photometric results (95% agreement to 2MASS K-band fluxes) were obtained by performing PRF fitting on the BCD images with APEX. Array location dependent photometric correction weights were applied before PRF fitting to minimize systematic error in the point source extraction flux. The images were then corrected with the background matching routine, and outliers were eliminated by the mosaicker.

PRFs were created for 3.6 μm and 4.5 μm data using the PRF estimate routine provided in APEX. At least twenty stars were chosen to make each PRF in areas with the smallest amount of crowding. The PRFs provided by the *Spitzer* Science Center (SSC)[3] that were made in-flight in January 2005 for 5.8 μm and 8 μm are sufficiently over-sampled, so there was no need to create new PRFs for these channels. Probable point sources with fluxes at least 4-σ above the background were then identified and selected for extraction on coadded images that had been corrected for array distortion. Final flux extractions were performed at these world coordinates positions on the corrected BCD images using PRF subtraction.

After applying the appropriate photometric color correction (as discussed in the IRAC Data Manual, v3.0) and comparing APEX 3.6 μm fluxes with 2MASS K-band fluxes (Skrutskie et al. 2006), the average [K - 3.6 μm] color is that of a K0 giant star. If we then assume that the majority of the stars we detect with *Spitzer* are K0 giant stars, then our fluxes are consistent with 2MASS K-band fluxes to within approximately 5%. To further check our photometric results, we compared the fluxes from thirty of the stars we detect to K-band fluxes from Cohen et al. (2005). The median [K-3.6 μm] color for these sources is 0.09, which is also consistent with K0 giant stars (See Fig. 2).

Color-magnitude diagrams (CMDs) derived from the IRAC point source photometry are presented in Fig. 3. An RGB is clearly evident with the tip occurring near $F_{3.6} = 14$ mJy. Stars with 3.6 μm flux > 11.2 mJy are possibly saturated in the long exposure frames, so only medium exposure (10.4 second) BCDs were used for the PRF subtractions and flux extraction. Flux densities for stars with colors redward of the RGB are listed in Table 3 (See §3.1).

[3]http://ssc.spitzer.caltech.edu/irac/psf.html

2.2. MIPS

The MIPS Data Analysis Tool (DAT, Gordon et al. (2005)) version 2.96 was used to do the basic processing and final mosaicking of the individual MIPS images. In addition, extra processing steps on each image were carried out before mosaicking using programs written specifically to improve the removal of MIPS detector instrumental signatures. At 24 μm the extra steps included readout offset correction, scan mirror dependent flat fields, a scan mirror independent flat field, array averaged background subtraction, and exclusion of the bias boost images. At 70 μm the extra steps were column average subtraction and pixel time filtering both with the exclusion of the regions around the bright sources. The pixel sizes of the final mosaics are 1.245″ and 4.925″ for 24 μm and 70 μm, respectively. The 24 μm mosaic covers a 90 square arcminute area and the 70 μm mosaic covers a 5.0 arcminute $\times$ 10.0 arcminute area, each centered on the core of M15.

The MIPS mosaics (Fig. 1b, c) show a possible ICM detection at 24 μm and 70 μm. The 24 μm image shows two high surface brightness patches of material, both offset from the core by $\simeq$ 17″ towards the west (IR1b and IR2). The 70 μm image shows only one high surface brightness patch that is likely an unresolved image of both 24 μm regions. The integrated fluxes of the ICM detections at both wavelengths were determined using basic aperture photometry in IDL v6.0. A 130.5″ square aperture centered at RA[J2000] = $21^{\rm h}$:$29^{\rm m}$:56″.50; Dec[J2000] = +12°:09′:53″.32 yields fluxes of 159.4±0.1 mJy at 24 μm and 691.2±61.0 mJy at 70 μm. The 70 μm flux agrees well with that found by Evans et al. (2003) with *ISO* observations using the same aperture size and position (Table 4). Also visible in the MIPS mosaics are the planetary nebula at 24 μm and several dust enshrouded stars, some of which are also visible in the 8 μm image, that may or may not be associated with the cluster.

Point source photometry was performed on the 24 μm mosaic using StarFinder (Diolaiti et al. 2000), which is well suited for the stable and well sampled MIPS 24 μm PSF. A STinyTim (Krist 2002)[4] model PSF with a temperature of 100 K and smoothed to account for pixel sampling was used for the stellar extractions. It has been shown that the smoothed STinyTim PSFs are excellent matches to observed MIPS 24 μm PSFs (Engelbracht et al 2006). CMDs comparing 24 μm to 3.6 μm and 8 μm are presented in Fig. 4, and the uncertainties in the IRAC and MIPS photometry are summarized in Fig. 5.

[4]http://ssc.spitzer.caltech.edu/archanaly/contributed/stinytim.tar.gz

2.3. IRS

Associated with our imaging programs, observations of the PN K648 (Pease 1928; Howard et al. 1997; Alves et al. 2000) in M15 were obtained with the *Spitzer* Infrared Spectrograph (IRS) on 2005 November 17.77 UT using the short wavelength (5-15 μm), low resolution module (SL) in staring mode. All observations utilized the IRS blue peak up array at the target position of the PN, RA[J2000] = $21^{\rm h}$:$29^{\rm m}$:$59''.41$; Dec[J2000] = $+12^{\circ}$:$10'$:$25''.70$, and the entire Hα nebulosity of K648 (cf. Fig. 2 of Alves et al. (2000)) was contained within the spectrograph slit. The slit dimensions are $57'' \times 3.6''$, and the slit was oriented 18.92 degrees west of north. The SL spectroscopic astronomical observing templates consisted of 5 cycles of 60 second ramps. IRS BCDs were processed with version 13.0.1 of the IRS pipeline. A description of the IRS instrument and its operation is available in Houck et al. (2004). Details of the calibration and raw data processing are specified in the IRS Pipeline Description Document, v1.0.[5]

Post-pipeline processing was conducted to remove instrumental artifacts, perform background subtractions and to combine extracted spectral segments. Fatally bad pixels were interpolated over in individual BCDs using bad pixel masks provided by the SSC. Multiple data collection events were obtained at two different positions on the slit using *Spitzer's* nod functionality. The two-dimensional BCDs were differenced to remove the background flux contribution and then the data were extracted with the *Spitzer* IRS Custom Extractor (SPICE) (v1.1-beta15)[6] using the default point source extraction widths. The extracted, background corrected data were combined using a weighted linear mean into a single output data file and clipped at the 3σ level. At the time of reduction, the errors generated by the SSC pipeline were not reliable enough for sound interpretation and so the errors were estimated from the standard deviation of the flux at each wavelength bin. Where there were less than three points in a wavelength bin, the error is the quadrature sum of the errors in the files. The resultant spectrum is presented in Fig. 6 and derived line fluxes are summarized in Table 5. The spectral lines were fitted using a least squares Gaussian routine that fits the line center, line amplitude, continuum amplitude and the slope of the continuum. The full-width half-maximum was fixed at the resolution limit of the low resolution module. Integrating the flux over the 8 μm IRAC bandpass yields a flux that agrees with the IRAC flux within the uncertainty limits. The strongest line in the mid-IR spectrum is the [Ne II]$\lambda = 12.81$ μm line, followed by hydrogen recombination lines H I $6-5$ (Pfα)$\lambda = 7.46$ μm and H I $7-6$ (Huα)$\lambda = 12.37$ μm. Emission from S^{3+} is evident

[5]http://ssc.spitzer.caltech.edu/irs/dh/PDD.pdf

[6]http://ssc.spitzer.caltech.edu/postbcd/doc/spice.gui_manual.html

in the spectrum, although the fit to the line flux of the [S IV]$\lambda = 10.52$ μm is of marginal signal-to-noise (S/N $\approx$ 2.3), while no [Ar III]$\lambda = 8.99$ μm is seen. Our detections of the mid-IR neon and sulfur lines are the first reported in the literature for K648. Abundance estimates derived from these forbidden lines are discussed in §3.2.

3. DISCUSSION

Our *Spitzer* images of M15 for the first time clearly show both the stellar dust producers and the ICM dust (Fig. 1), allowing a direct comparison to be made between the dust injection and dust survival rates. The brightest source of 70 μm emission, IR1a, is blended at 70 μm but visible as separate objects in the MIPS 24 μm map, IR1b and IR2. These sources are completely invisible on the IRAC maps, even at 8 μm. A three color image of 8, 24, and 70 μm in which the 8 and 24 μm images are degraded to match the 70 μm resolution is presented in Fig. 7. This figure illustrates that IR1a is not unresolved stellar emission, but is a starless dust cloud(s) that are likely to be of an intra-cluster nature. The next brightest objects at 70 μm are a pair of sources, IR3a and IR3b, that are situated at the fringes of the cluster and may not be physically associated with the cluster. IR3b was previously detected by 2MASS, but there are no known previous detections of IR3a. The probability of detecting non-member red sources in the field are sufficiently small to suggest that these sources are associated with the cluster. The only other 70 μm source, IR4, is also located on the fringes of the cluster. Radial velocity measurements from Pilachowski et al. (2000) confirm its membership. Table 3 lists fluxes for IR3a, IR3b, IR4, and other possibly dusty sources, described in §3.1. All three of these sources have mid-IR colors that are consistent with post-AGB stars (Fig. 4; Groenewegen (2006)). In addition to these sources, the planetary nebula K648 (Ps 1) is also detected in all IRAC bands and at 24 μm. The strong 24 μm dectection is likely due not only to dust, but also to line emission from [O IV] at 25.88 μm and/or [Fe II] at 25.98 μm.

3.1. Mass-Losing Stars

Figure 8 shows the locations of the mass-losing AGB stars in M15. The coordinates and IRAC fluxes of these sources are listed in Table 3. These stars were identified by their locations on the IRAC CMDs (Fig. 3), redward of the RGB. We find 24 mass-losing/dust-enshrouded stars and consider this a lower limit (due to potential source confusion) of the total number in the cluster. These stars also fall just redward of the RGB in the MIPS CMDs as well, which suggests that they could be post-AGB stars. Their IRAC colors, however,

indicate that it is more likely that they are AGB stars that are approaching the end of the AGB phase of their evolution (Groenewegen 2006). The stars blueward of the RGB can be explained by the absorption in the fundamental bands of CO in the 4.5 μm band and SiO in the 8 μm band. The red, mass-losing stars in M15 populate an uneven spatial distribution about the core of the cluster as projected on the sky (Fig. 8). These stars are offset from the core in the same sense as IR1a, IR1b, and IR2, and the distribution is less cusped than the visual light. Since M15 is 13.2 Gyr old (McNamara et al. 2004), most stars currently on the AGB have a zero-age MS mass of $\simeq 0.8$ M$_\odot$. These stars will soon end their lives as white dwarfs of $\simeq 0.5$ M$_\odot$, having lost approximately 0.3 M$_\odot$ during their post-main sequence evolution. The loose spatial distribution of this population could therefore be due to mass segregation, in which lower-mass stars are displaced to the outer regions of the cluster due to their high velocities, leaving a preferential concentration of high-mass stars near the center of the potential well of the cluster (Spitzer 1987).

The MIPS CMDs (Fig. 4) identify a population of approximately 23 post-AGB stars (Groenewegen 2006). The colors of IR3a, IR3b, and IR4 are similar to the colors of this population. These stars are bright at 24 μm, but they are not detected above the background at 70 μm (Table 3). They are distributed around the cluster center at an average radius of approximately 3.3$'$, and their positions are biassed towards the southern side of the cluster, near IR3a, IR3b, and IR4. Mass segregation is most likely responsible for their locations at the fringes of the cluster.

Although M15 is one of the most massive galactic globular clusters, it is surprising to find many dusty objects, as the cluster metallicity of [Fe/H] $= -2.4$ places it amongst the most metal-poor galactic globular clusters. Dust forms from metal condensates and it is difficult to understand how dust grains can form at such low metal abundances. It is likely that the metals condensing to form dust are produced in the stars themselves and brought to the surface near the end of their evolution. The fact that dust production does not seem to be inhibited at metallicities $\lesssim 1\%$ solar implies that stellar mass loss must already have contributed dust very early on in the evolution of the Universe. Dust observed at high redshift is usually believed to originate in supernovae explosions that result from core collapse in massive stars, but our observations suggest that at least some of the dust formed within the first few 100 million years may have been produced by stars of only a few solar masses (e.g. MS lifetime from models by Vassiliadis & Wood (1993)).

Various investigators (Daulton et al. 2002; Amari et al. 2001) suggest that dust grains can form more easily at low metallicity in carbon stars, as these stars produce carbon themselves. With less initial oxygen abundance to start with, it is easier for these stars to achieve C/O > 1 in their carbon shells. With excess carbon available (after locking up equal amounts

of C and O in CO), formation of carbon-chain molecules from which dust grain condensation can proceed. However, although there is evidence for high molecular abundances in stellar atmospheres at low metallicity, dust production in these stars may be less efficient due to a lack of SiC seeds (Sloan et al. 2006). Furthermore, van Loon (2006) suggests that the low optical depth in carbon stars in the Magellanic clouds points against large dust-to-gas ratios at low metallicity.

For low-mass oxygen-rich stars, one would not expect this evolution to lead to effective dust production, as dredge-up only increases the C/O ratio and does not facilitate the formation of oxygen-rich dust grains. In any case, for oxygen-rich stars it is well established that nucleation sites must be available to condense dust grains onto (Jeong et al. 1999). These seeds are likely to be TiO or similar which include secondary elements that are not produced by the star itself. Other s-process seeds, such as Zr, may be dredged-up in the atmospheres of these stars, but the limiting factor for dust production with such seeds is the oxygen abundance, as more oxygen will be locked into CO after dredge-up. Unfortunately, our observations do not allow us to draw any conclusions as to the abundances of secondary elements in the mass-losing stars in M15.

The suspicion is that stars do adjust their structure until they finally can shed their mantles as demonstrated by K648 in M15. From the analysis of spectra of GC giant stars, a picture is emerging in which metal-poor stars do become very cool while nonetheless exhibiting early-type spectra because the low metal abundances give rise to weak absorption. They may not form much dust, but they may still be able to form enough of it to drive a wind. The mid-IR spectrum of 47 Tucanae V1 suggests typical silicate dust grains and a typical mass loss rate of 10^{-6} $M_{\odot}$ yr^{-1} (van Loon et al. 2006).

3.2. IR Spectrum of K648

Although UV and optical line ratios derived for K648 from previous investigations provide constraints on relative abundance ratios, several important α-capture elements, such as S, Ar, and Ne, have ground configurations that produce only IR fine-structure. If lines from these ions are not observed and introduced into abundance models, the total abundance of these elements becomes uncertain (Dinerstein et al. 2003). Often, measuring emission line flux from [Ne II]λ12.81 μm, [S IV]λ10.51 μm, and [Ar III]λ8.99 μm is observationally challenging from the ground. However, the sensitivity of the *Spitzer* IRS affords an opportunity to set stringent limits on the emission line flux of these ions resulting in better constrained estimates on derived abundances. In addition, new radiative transition rates and collision strengths are now available as a result of the IRON project (Hummer et al. 1993) to improve

the accuracy of derived abundance ratios. Below, we discuss the analysis of our *Spitzer* measurements (Table 5) of the [S IV] and [Ne II] lines in K648 and present a reanalysis of the S/O and Ne/O ratios with contemporary atomic parameters using a simple model. Undertaking a full photoionization analysis of K648 (i.e., Howard et al. (1997)) using the *Spitzer* IR line fluxes is beyond the scope of this paper.

3.2.1. Hβ

Accurate extinction correction of UV and optical lines with respect to Hβ are required for abundance determinations. Interstellar extinction estimates to K648 range from $0.2 \leq A_V \leq 0.6$ (Garnett & Lacy 1993). However, at mid-IR wavelengths, extinction is minimal ($\lesssim 0.02$ mag), and the Pfα and Huα lines detections (Fig. 6) enable us to estimate the emitted Hβ flux directly. Assuming Case B (Osterbrock 1999), and adopting a $T_e = 12,500$ K and density of $\approx 10^3$ cm^{-1} (Garnett & Lacy 1993) we derived $F(\mathrm{H}\beta) = (1.91 \pm 0.30) \times 10^{-12}$ ergs cm^2 s^{-1} and $F(\mathrm{H}\beta) = (1.13 \pm 0.36) \times 10^{-12}$ ergs cm^2 s^{-1} from the Pfα and Huα lines respectively using the intrinsic hydrogen emissivity ratios tabulated in Hummer & Storey (1987). These two estimates are in reasonable agreement (within the formal error) with each other, considering there is an absolute photometric uncertainty of $\approx 5\%$ (Houck et al. 2004) between the two spectral orders ($5.2 - 8.7$ μm and $7.4 - 14.0$ μm). Our average $F(\mathrm{H}\beta)$ of $(1.52 \pm 0.23) \times 10^{-12}$ ergs cm^2 s^{-1} is in good agreement with previous observational estimates, especially those obtained with large apertures (Garnett & Lacy 1993), and we will adopt this value in our abundance analysis.

3.2.2. Neon

The ratio of [Ne II]$\lambda = 12.81$ μm line flux to our derived average value of Hβ was used to estimate the Ne^+/H^+ abundance. We have adopted a collisional strength $\Upsilon(\mathrm{T}) = 0.283$ (appropriate for $\mathrm{T}_e = 10^4$ K, Saraph & Tully (1994)) and an A_{if} value of 8.59×10^{-3} s^{-1} from the NIST database and assumed an electron density of $N_e = 1.7 \times 10^3$ cm^{-3} (Garnett & Lacy 1993). Rate coefficients, q_{fi} (Hummer et al. 1993) and the population levels were computed assuming Ne^+, a $2p^5$ ion, is a two-level atom. Following Rank et al. (1978), we define the relative abundance of Ne^+/H^+ as

$$\frac{Ne^+}{H^+} = \frac{(4\pi\ j_{H\beta}/N_e N_p)N_e}{h\nu_{fi} A_{if} f_f} \times \frac{I([\mathrm{Ne\ II}])}{I(H\beta)}, \tag{2}$$

where the Hβ volume emissivity, $4\pi j_{H\beta}/N_e N_p$, is 1.0301×10^{-25} erg cm^3 s^{-1} interpolated for the assumed N_e (Hummer & Storey 1987), $f_f = 9.86 \times 10^{-4}$ is the population ratio of the upper to lower state, and I([Ne II]), the observed neon line flux, is $(1.74 \pm 0.08) \times 10^{-13}$ erg cm^{-2} s^{-1} (Table 5). This yields a ratio of $Ne^+/H^+ = (1.53 \pm 0.21) \times 10^{-5}$. The relative abundance of Ne^{2+}/H^+ was estimated from optical measurements of the [Ne III]λ3869 Å and [Ne III]λ3967 Å lines (Adams et al. 1984) and de-reddened assuming $c = 0.12$ and a Seaton (1979) extinction law. Using the [Ne III] to Hβ ratios (see Table 6), the relative populations were computed using a multi-level atom program incorporating the best available $A_{ij}(s^{-1})$ and collision strengths available from the NIST database and the literature (Moore, Hester, & Dufour 2004), which is similar to code originally described by Shaw & Dufour (1995). Summing over all ions, we find a total Ne/H= $(2.39 \pm 0.27) \times 10^{-5}$ and a Ne/O $= 0.48 \pm 0.14$ adopting an O/H $= (5.0 \pm 1.3) \times 10^{-5}$ (Peña et al. 1993).

3.2.3. Sulfur

The relative sulfur abundance was computed in a similar manner as the neon abundance described in §3.2.2, although all relative populations were determined using the (Moore, Hester, & Dufour 2004) code. The *Spitzer* observation of [S IV] was used to determine the S^{3+}/H^+ population, while the optical fluxes reported by (Barker et al. 1983) corresponding to Hβ (assuming $j(H\alpha)/j(H\beta) = 2.81$; Osterbrock (1999)) were used to estimate the relative S^{2+}/H^+ and S^+/H^+ abundances (Table 6). We find an upper limit to the total S/H of $(4.28 \pm 1.28) \times 10^{-8}$, which is ≈ 2.5 lower than that inferred by Garnett & Lacy (1993). Adopting an O/H $= (5.0 \pm 1.3) \times 10^{-5}$ (Peña et al. 1993), yields a S/O $= (8.56 \pm 3.39)^{-4}$.

3.2.4. Abundance Comments

Our new estimates of the [S/O]≤ -2.64 and [Ne/O] $= +0.54$ confirm that K648 is under-enriched in S as compared to O (Garnett & Lacy 1993), while Ne/O is enhanced with respect to solar. The Ne enhancement is seen in other halo population PNe, such as BB-1 (Dinerstein et al. 2003). Garnett & Lacy (1993) argue that contamination of He-burning products by α-captures at high temperature could account for enhanced Ne. Bianchi et al. (2001), based on analysis of *Hubble Space Telescope* (HST) *Faint Object Spectrograph* (FOS) spectra of the central star, suggest that the nebular shell was ejected by a low-mass He-burning progenitor that has subsequently undergone a late thermal pulse, perhaps similar to the evolution of objects akin to FG Sge (Gehrz et al. 2005). Our derived neon abundance using the fine structure line, suggests that dredge-up from the stellar core may

be an important mechanism to pollute the expelled nebular materials from slowly evolving, young PNe.

3.3. Dust in the ICM

Assuming that the diffuse emission detected in the *Spitzer* images arises from ICM material, we can compute a dust mass using the observed SEDs. The approximate temperature of the ICM dust was derived by least-squares fitting a greybody model to the SED using fluxes measured in a 130.5 × 130.5 square arcsecond aperture centered at the same right ascension and declination coordinates in images at all wave bands. Our choice of aperture size is equivalent to that used by Evans et al. (2003) to facilitate direct comparison. The large wavelength range of the *Spitzer* SED enables us to distinguish between the contribution of a stellar blackbody (peaking near 0.64 μm and dominated by K0 stars), and that of thermal radiating dust that generates an IR excess at wavelengths greater than 24 μm. Use of a two-component model, incorporating a stellar blackbody that peaks near 4699 ± 58 K and a dust blackbody that peaks near $T_d = 70 \pm 2$ K, gives a rough fit to the data (Fig. 9; Table 4). The fit produces a large reduced χ^2 value of 5.26 suggesting that the integrated flux within our aperture sums the emission from stars of many disperate spectral types not well-represented by a simple, single emissivity and temperature blackbody. Another source of uncertainty in the fit is the effect of crowding in 2MASS data. This could lead to oversubtraction of the background and overestimation of the flux densities (van Loon et al. 2005).

The mass of the ICM was determined using the methodology described in Evans et al. (2003). We assume that the dust is optically thin, which yields the following expression

$$\frac{M_d}{M_\odot} = 4.79 \times 10^{-17}\ f_\nu(mJy)\ \frac{D_{kpc}^2}{\kappa_\nu B(\nu, T_d)}, \tag{3}$$

where D_{kpc} is the distance to M15 in kiloparsecs (Table 1), κ_ν is the dust absorption coefficient in cm^2 g^{-1}, $B(\nu, T_d)$ is the Planck function in cgs units, and T_d is the dust temperature. f_ν at 70 μm is 691.2 ± 61.1 mJy (Table 4), and κ_ν is taken from Ossenkopf & Henning (1994) to be 56 ± 11 cm^2 g^{-1} at 70 μm, assuming a standard MRN dust distribution (Mathis et al. 1977) and an ISM-type composition consisting of graphite and silicate grains. We derive a total dust mass of $(9 \pm 2) \times 10^{-4}$ M$_\odot$, which agrees within a factor of two compared to the value cited by Evans et al. (2003) of $(4.8 \pm 1.6) \times 10^{-4}$ M$_\odot$, and is approximately 2-4 times smaller than the dust mass predicted by equation (1). The discrepancy between the *Spitzer* and *ISO* calculated dust masses may be largely due to the different choice of κ_ν, as the ICM flux densities at 70 μm agree within the errors stated (Table 4). κ_ν is the most uncertain

parameter in the dust mass estimate, as its value depends largly on composition and density assumptions. Therefore, we note that κ_ν could be up to an order of magnitude larger than the value we have invoked here.

The diffuse emission from ICM dust in M15 is located approximately 17″ to the west of the cluster core. The paucity of diffuse dust toward the cluster center, where the gravitational potential well is steepest, is puzzling. One possible explanation for this asymmetry is a collection of millisecond pulsars (PSRs) near the core of M15 (Sun et al. 2002). Seven PSRs are located within 17″ of the core (Fig. 10), and the radiative environs associated with these objects could lead to destruction of dust grains by sputtering or other ablation processes and may also inhibit dust production in stellar winds. The PSR nearest to the ICM dust distribution observed in the MIPS image, PSR2129+1210F, is located on the northeast outer edge of the 70 μm emission (Taylor et al. 1993). If, on the other hand, each mass-losing star has contributed 0.15 $M_\odot$ to the ICM on average (assuming that each star will lose 0.3 $M_\odot$ over its entire lifetime), then we see that an ICM dust mass of 1×10^{-3} $M_\odot$ corresponds to mass lost from $\sim 10^2$ stars. This suggests that the ICM is short-lived, as this many stars will have passed through the AGB superwind phase, defined as the phase in which the mass loss rate exceeds the nuclear burning mass consumption rate (van Loon et al. (1999) suggests $\dot{M} \sim 10^{-4} - 10^{-5}$ $M_\odot$ yr^{-1} for low-mass stars), in only $\approx 10^6$ yr, which is much shorter than the cluster's relaxation timescale. The ICM dust therefore cannot be expected to have relaxed and assumed the global shape of the gravitational potential well. If this is the case, the offset of the dust cloud from the center of the cluster would not come as a surprise.

Sources of the ICM dust include the post main sequence mass-losing stars identified in Fig. 8. If we assume that the dust-to-gas ratio scales in proportion to metallicity during the superwind phase, as indicated by Marshall et al. (2004), then at the metallicity of M15, a dust mass loss of 10^{-10} $M_\odot$ yr^{-1} is expected (Becker 2000). With this mass loss rate, we again find that the dust has been accumulating for approximately 1×10^6 years, significantly shorter than the time between subsequent passages of the galactic plane (Evans et al. 2003). This short time scale suggests that dust does not survive long in the ICM. Processes that could be responsible for removing dust from the ICM include ram pressure by the galactic halo gas, radiation-driven outflow or photo-destruction.

4. CONCLUSIONS

Analysis of our *Spitzer* image data on the core of the globular cluster M15 show strong evidence for the presence of intercluster medium (ICM) dust in the cluster core, with a mass of $(9 \pm 2) \times 10^{-4}$ $M_\odot$ and with an equilibrium temperature of ≈ 70 K. This is the first secure,

high signal to noise detection of ICM dust in a globular cluster. Also present surrounding the core are populations of dusty AGB and post-AGB stars, along with the planetary nebula K648. Using IRS spectral data, we have observed both the [S IV] and [Ne II] fine structure lines in K648 and have derived abundance estimates.

The unique capabilities of *Spitzer* have enabled us to identify both the interstellar dust and the dust producers in M15. This is surprising at such low metallicity ([Fe/H] = -2.4), and may have implications for dust production in the early universe. The mass of the ICM dust in M15 suggests that it has been accummulating for $\sim 10^6$ years, which is a factor of ten shorter than the time since the last galactic plane crossing. The dust mass is also approximately 4 times smaller than the mass predicted by Evans et al. (2003). Both of these results imply that such dust does not survive long compared to its production rate, and is thus part of a stochastic process.

We acknowledge helpful discussions with G. Schwarz and B. Moore regarding approaches to abundance modeling in PNe, and BDM for providing source code for multi-level atom calculations. M. L. B., C, E. W., L. A. H., E. P., and R. D. G. are supported in part by NASA through *Spitzer* contracts 1256406, 1215746, 1268006, and 1276760 issued by JPL/Caltech to the University of Minnesota, and by National Science Foundation grant AST02-05814. This publication makes use of data products from the Two Micron All Sky Survey, which is a joint project of the University of Massachusetts and the Infrared Processing and Analysis Center/California Institute of Technology, funded by the National Aeronautics and Space Administration and the National Science Foundation.

REFERENCES

Adams, S., Seaton, M. J., Howarth, I. D., Auriére, M., & Walsh, J. R. 1984, MNRAS, 207, 471

Alves, D. R., Bond, H. E., & Livio, M. 2000, AJ, 120, 2044

Amari, S., et al. 2001, ApJ, 546, 248

Auriére, M., Le Févre, O., & Terzan, A. 1984, A&A, 138, 415

Barker, T. 1983, ApJ, 270, 641

Becker, S. A. 2000, in *Astrophysical Quant.,*, 4th edition, eds. A.N. Cox, [AIP Press: New York], p.515

Bianchi, L., et al. 2001, AJ, 122, 1538

Birkinshaw, M., Ho, P. T. P., & Baud, B. 1983, A&A, 125, 271

Charles, P. A., Jones, D. C., & Naylor, T. 1986, Nature, 323, 417

Cohen, J. G., Briley, M. M., & Stetson, P. B. 2005, AJ, 130, 1177

Condon, J. J., Cotton, W. D., Greisen, E. W., Yin, Q. F., Perley, R. A., Taylor, G. B., & Broderick, J. J. 1998, AJ, 115, 1693

Daulton, T. L., et al. 2002, Science, 296, 1852

Diolaiti, E., Bendinelli, O., Bonaccini, D., Close, L., Currie, D., & Parmeggiani, G. 2000, A&AS, 147, 335

Dinerstein, H. L., Richter, M. J., Lacy, J. H., & Sellgren, K. 2003, AJ, 125, 265

Engelbracht, C. W., et al. 2006, in prep.

Evans, A., Stickel, M., van Loon, J. Th., Eyres, S. P. S., Hopwood, M. E. L., & Penny, A. J. 2003, A&A, 408, L9

Faulkner, D. J., Scott, T. R., Wood, P. R., & Wright, A. E. 1991, ApJ, 374, L45

Fazio, G. G., et al. 2004, ApJS, 154, 10

Forte, J. C., Bassino, L. P., Vega, E. I., Pellizza González, L. J., Cellone, S. A., & Méndez, M. R. 2002, AJ, 123, 3263

Freire, P. C., Kramer, M., Lyne, A. G., Camilo, F., Manchester, R. N., & D'Amico, N. 2001, ApJ, 557, L105

Garnett, D. R., & Lacy, J. R. 1993, ApJ, 419, L93

Gehrz, R. D., Woodward, C. E., Temim, T., Lyke, J. E., & Mason, C. 2005, AJ, 623, 1105

Gillett, F. G., de Jong, T., Neugebauer, G., Rice, W. L., & Emerson, J. P. 1988, AJ, 96, 116

Gordon, K. D., et al. 2005, PASP, 117, 503

Groenewegen, M. A. T. 2006, A&A, 448, 181

Hopwood, M. E. L., Evans, A., Penny, A., & Eyres, S. P. S. 1998, MNRAS, 301, L30

Hopwood, M. E. L., Eyres, S. P. S., Evans, A., Penny, A., & Odenkirchen, M. 1999, A&A, 350, 49

Houck, J., et al. 2004, ApJS, 154, 10

Howard, J. W., Henry, R. B. C., & McCartney, S. 1997, MNRAS, 284, 465

Hummer, D. G., & Storey, P. J. 1987, MNRAS, 224, 801

Hummer, D. G., Berrington, K. A., Eissner, W., Pradhan, Anil K., Saraph, H. E., & Tully, J. A. 1993, A&A, 279, 298

Indebetouw, R., et al. 2005, ApJ, 619, 931

Jacoby, G. H., Morse, J. A., Fullton, L. K., Kwitter, K. B., & Henry, R. B. C. 1997, AJ, 114, 2611

Jeong, K. S., Winters, J. M., & Sedlmayr, E. 1999, IAU Symp. 191: Asymptotic Giant Branch Stars, 191, 233

Krist, J. 2002, *Tiny Tim/SIRTF User's Guide*, [Pasadena, CA: SSC]

Kulkarni, S. R., & Anderson, S. B. 1996, IAU Symp. 174: Dynamical Evolution of Star Clusters: Confrontation of Theory and Observations, 174, 181

Makovoz, D., & Marleau, F. R. 2005, PASP, 117, 1113

Marshall, J. R., van Loon, J. T., Matsuura, M., Wood, P. R., Zijlstra, A. A., & Whitelock, P. A. 2004, MNRAS, 355, 1348

Mathis, J. S., Rumpl, W., & Nordsieck, K. H. 1977, ApJ, 217, 425

McNamara, B. J., Harrison, T. E., & Baumgardt, H. 2004, ApJ, 602, 264

Moore, B. D., Hester, J. J., & Dufour, R. J. 2004, AJ, 127, 3484

Odenkirchen, M., Brosche, P., Geffert, M., & Tucholke, H.-J. 1997, New Astronomy, 2, 477

Origlia, L., Ferraro, F. R., Fusi Pecci, F., & Rood, R. T. 2002, ApJ, 571, 458

Ossenkopf, V., & Henning, Th. 1994, A&A, 291, 943

Osterbrock, D. E. 1999, *Astrophysics of Gaseous Nebulae and Active Galactic Nuclei,* [Mill Valley, CA: Univ. Sci.]

Pease, F. G. 1928, PASP, 40, 342

Peña, M., Torres-Peimbert, S., Peimbert, M., & Dufour, R. J. 1993, Revista Mexicana de Astronomía y Astrofísica, vol. 27, 175

Phinney, F. S. 1996, ASP Conf. Ser. 90: The Origins, Evolution, and Destinies of Binary Stars in Clusters, 90, 163

Pilachowski, C. A., Sneden, C., Kraft, R. P., Harmer, D., & Willmarth, D. 2000, AJ, 119, 2895

Ramdani, A., & Jorissen, A. 2001, A&A, 372, 85

Rank, D. M., Dinerstein, H. L., Lester, D. F., Bregman, J. D., Aitken, D. K., & Jones, B. 1978, MNRAS, 185, 179

Rieke, G. H., & Lebofsky, M. J. 1985, ApJ, 288, 618

Rieke, G. H., et al. 2004, ApJS, 154, 25

Saraph, H. E., & Tully, J. A. 1994, A&AS, 107, 29

Schlegel, D. J., Finkbeiner, D. P., & Davis, M. 1998, ApJ, 500, 525

Seaton, M. J. 1979, MNRAS, 187, 73P

Shaw, R. A., & Dufour, R. J. 1995, PASP, 107, 896

Skrutskie, M. F., et al. 2006, AJ, 131, 1163

Sloan, G. C., Kraemer, K. E., Matsuura, M., Wood, P. R., Price, S. D., & Egan, M. P. 2006, ArXiv Astrophysics e-prints, arXiv:astro-ph/0603607

Sneden, C., Kraft, R. P., Shetrone, M. D., Smith, G. H., Langer, G. E., & Prosser, C. F. 1997, AJ, 114, 1964

Spitzer, L. 1987, Princeton, NJ, Princeton University Press, 1987

Spitzer Science Center, IRAC Data Handbook, version 3.0 (Pasadena: SSC), http://ssc.spitzer.caltech.edu/irac/dh/iracdatahandbook3.0.pdf

Spitzer Science Center, IRS Pipeline Handbook, version 1.0 (Pasadena: SSC), http://ssc.spitzer.caltech.edu/irs/dh/PDD.pdf

Stetson, P.B. 1987, PASP, 99, 191

Sun, X.-H., Han, J.-L., & Qiao, G.-J. 2002, ChJAA, 2, 133

Taylor, J. H., Manchester, R. N., & Lyne, A. G. 1993, ApJS, 88, 529

Trams, N. R., et al. 1999, A&A, 346, 843

van Loon, J. Th., Zijlstra, A. A., Whitelock, P. A., Waters, L. B. F. M., Loup, C., & Trams, N. R. 1997, A&A, 325, 585

van Loon, J. Th., Groenewegen, M. A. T., de Koter, A., Trams, N. R., Waters, L. B. F. M., Zijlstra, A. A., Whitelock, P. A., & Loup, C. 1999, A&A, 351. 559

van Loon, J. Th., Zijlstra, A. A., & Groenewegen, M. A. T. 1999, A&A, 346, 805

van Loon, J. Th., Gilmore, G. F., Omont, A., Blommaert, J. A. D. L., Glass, I. S., Messineo, M., Schuller, F., Schultheis, M., Yamamura, I., & Zhao, H. S. 2003, MNRAS, 338, 857

van Loon, J. Th., Marshall, J. R., & Zijlstra, A. A. 2005, A&A, 442, 597

van Loon, J. Th. 2006, in: (eds.) Lamers, Langer, Nugis & Annuk, Stellar Evolution at Low Metallicity: Mass Loss, Explosions, Cosmology, ASP, in press astro-ph/051232

van Loon, J. Th., Stanimirović, S., Evans, A., & Muller, E. 2006, MNRAS, 365, 1277

Vassiliadis, E., & Wood, P. R. 1993, ApJ, 413, 641

Webbink, R. F. 1985, IAU Symp. 113: Dynamics of Star Clusters, 113, 541

Werner, M. W., et al. 2004, ApJS, 154, 1

Zijlstra, A. A., Loup, C., Waters, L. B. F. M., Whitelock, P. A., van Loon, J. Th., & Guglielmo, F. 1996, MNRAS, 279, 32

Fig. 1.— Three-color images of the core of M15 (NGC 7078) spanning 3.6 μm to 70 μm. The field shown is 3' × 6.3'. (a) Blue is 3.6 μm, green is 4.5 μm, and red is 8 μm. The PN (K648) becomes visible near the upper left of the cluster core. (b) Blue is 5.8 μm, green is 8 μm, and red is 24 μm. The intra-cluster medium (ICM) becomes visible as two resolved high surface brightness patches (IR2 & IR1b) off-center from the cluster core. Three dusty sources, IR3a, IR3b, and IR4, also become prominent at 24 μm.(c) Blue is 8 μm, green is 24 μm, and red is 70 μm. The two ICM clouds are no longer resolved at 70 μm (IR1a).

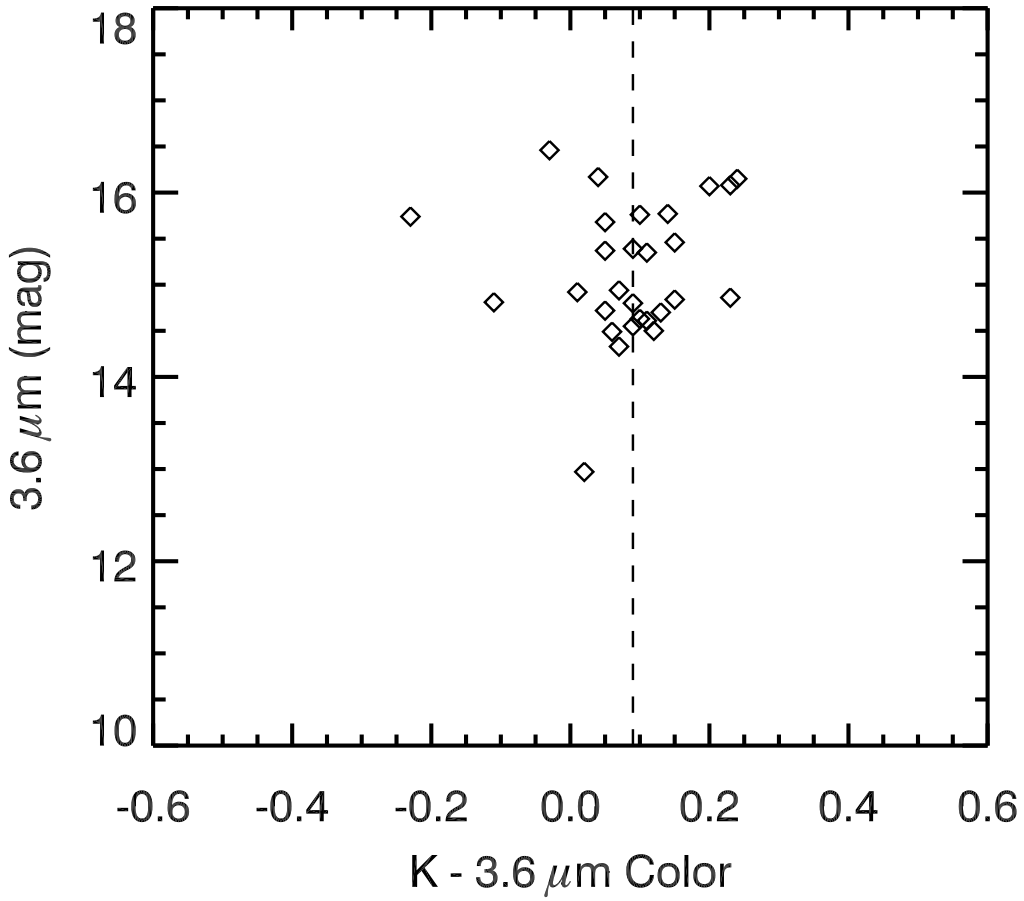

Fig. 2.— Color magnitude diagram showing [K–3.6 μm] colors. K magnitudes are from Cohen et al. (2005). The dashed line corresponds to the median color, which is consistent with K giant stars.

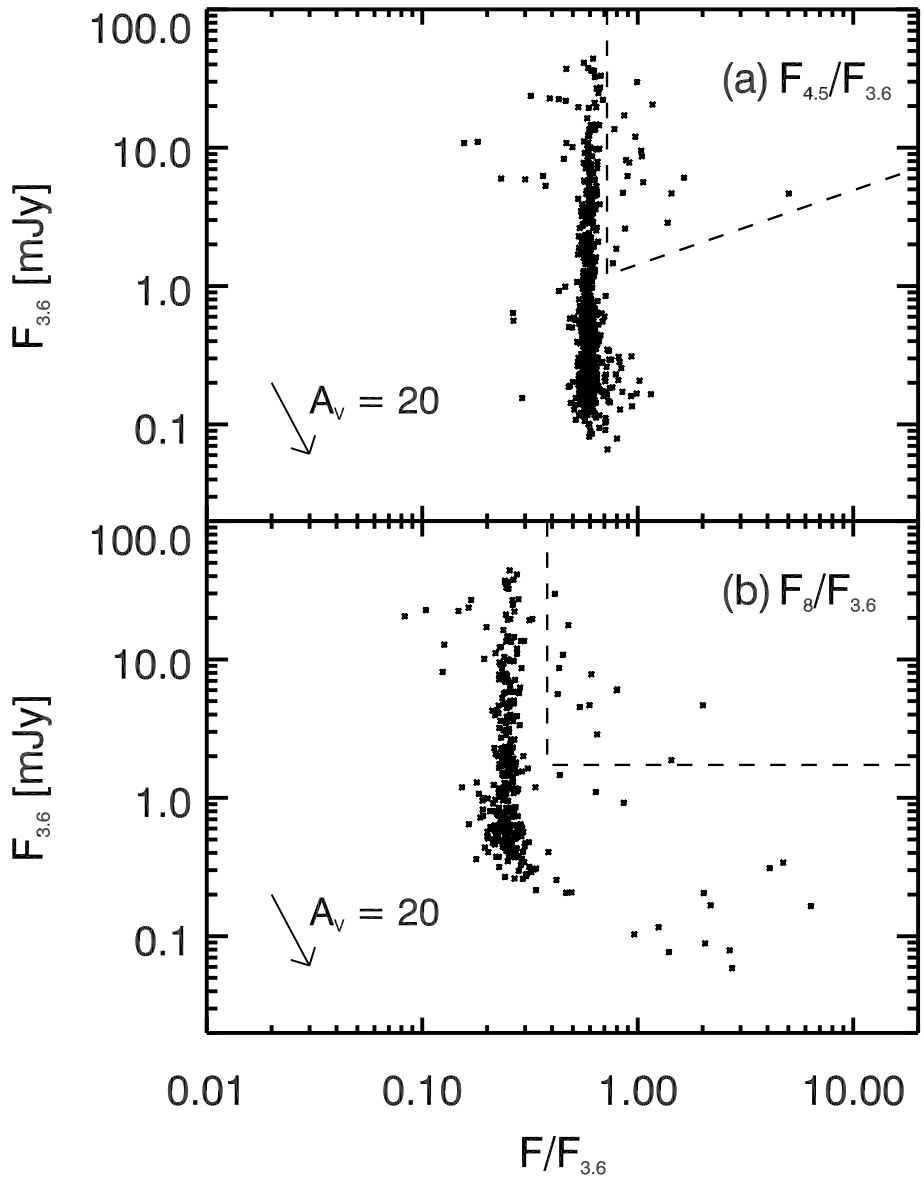

Fig. 3.— IRAC color magnitude diagrams (CMDs) for M15. Fluxes are not color corrected or dereddened. (a) CMD for 4.5 μm-3.6 μm color vs 3.6 μm flux. (b) CMD for 8 μm-3.6 μm color vs 3.6 μm flux. The uncertainties in the photometry are given in Fig. 5. The regions enclosed by the dashed lines (left of vertical, above horizontal) are the mass loss regions. The locations of these stars are plotted in Fig. 8, and their fluxes are listed in Table 3.

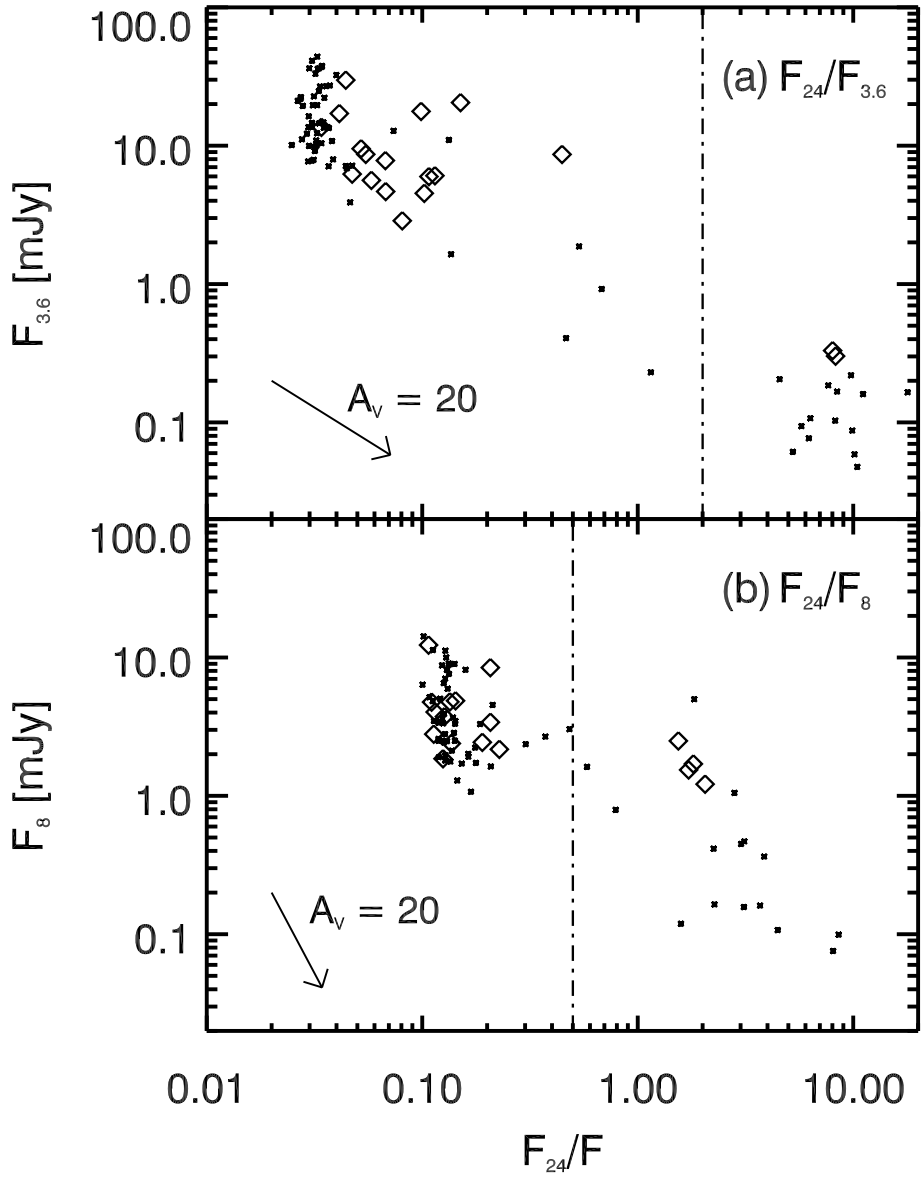

Fig. 4.— MIPs color magnitude diagrams (CMDs) for M15. Fluxes are not color corrected or dereddened. (a) CMD for 24 μm-3.6 μm color vs 3.6 μm flux. (b) CMD for 24 μm-8 μm color vs 8 μm flux (see Fig. 5 for uncertainties in the photometry). The diamonds mark the mass losing stars identified in Fig. 3. The dash-dot lines mark the approximate division between AGB and post-AGB stars (Groenewegen 2006). IR3a, IR3b, and IR4 each fall well within the post-AGB region in (b), while only IR3a and IR3b fall within the post-AGB region in (a). The IRAC colors of the other mass losing sources suggest that they are AGB stars.

Fig. 5.— Photometry errors for the IRAC 3.6, 4.5, 8, and MIPS 24 μm bands.

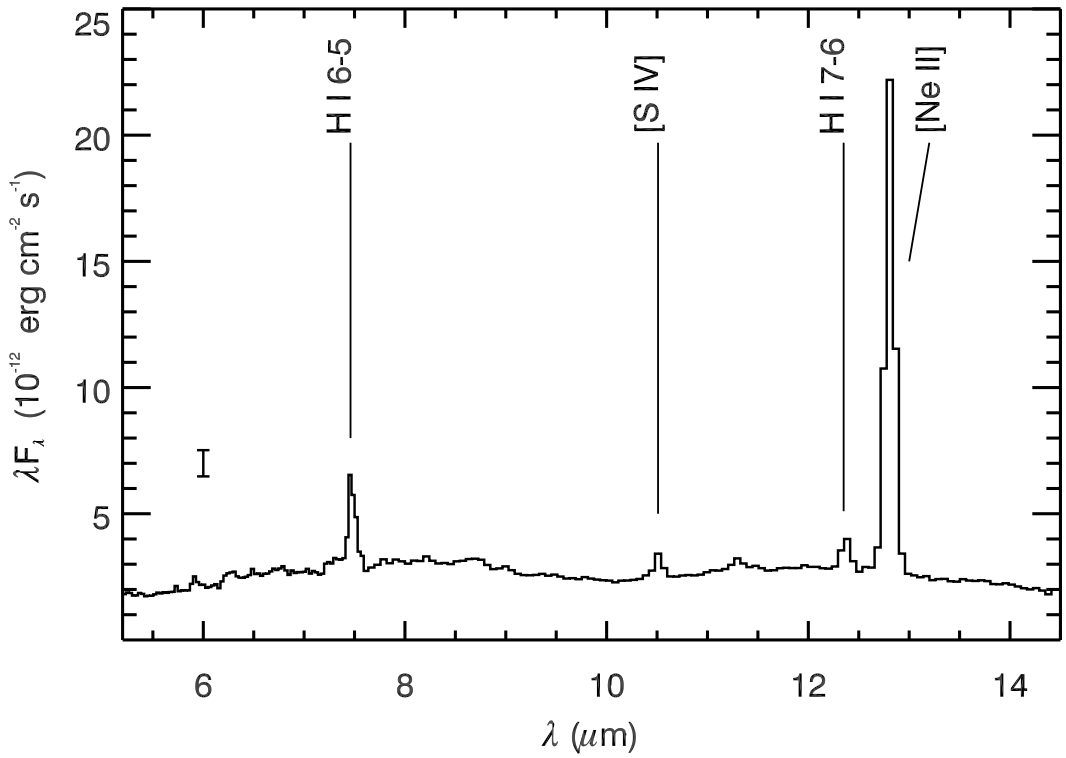

Fig. 6.— *Spitzer* IRS spectrum of the PN (K648) obtained with the short low (SL) module. The most prominent emission line in the spectrum is [Ne II]$\lambda = 12.81$ μm in addition to weak H recombination lines and the [S IV] line. The representative error bar (*left inset*) shows the average photometric uncertainty in the spectra. No strong dust continuum is evident in the IRS spectrum.

Fig. 7.— Three color image of 8 μm (blue), 24 μm (green), and 70 μm (red) images. The 24 μm and 8 μm images were rebinned to the 70 μm image pixel size of 4.925 arcseconds then convolved with the 70 μm *Spitzer* point response function (PRF). This image shows that the 70 μm emission is not unresolved stellar emission.

Fig. 8.— Locations of Mass-losing stars in M15. (a) the 3.6 μm mosaic and (b) the 24 μm mosaic. All of the stars marked are located redward of the RGB.

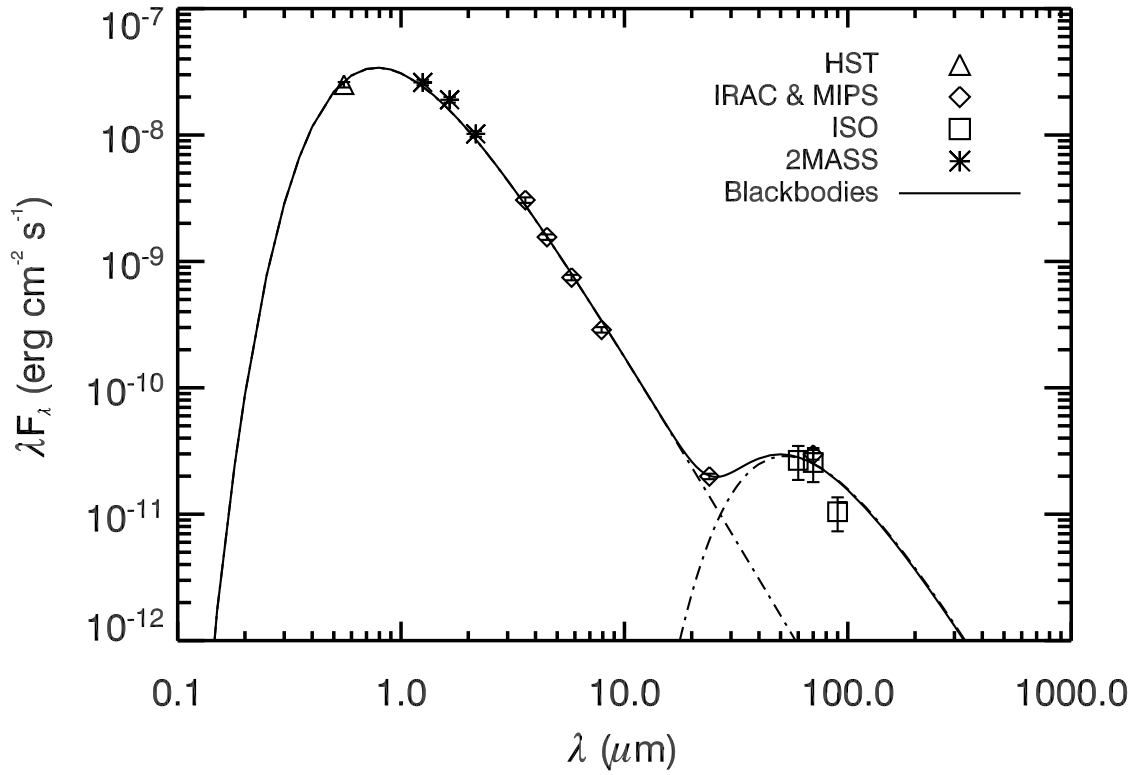

Fig. 9.— Spectral energy distribution (SED) of the stellar and dust components near the core of M15. Fluxes (see Table 4) were obtained by using a square aperture centered on the dust emission at *ISO* wavelengths. The best two-blackbody fit ($\chi^2 = 5.26$) yields 4698 $\pm$ 58 K and 70 $\pm$ 2 K for the stellar and dust components, respectively. The dash-dot lines are the individual blackbodies, while the solid line is the sum of the two blackbodies.

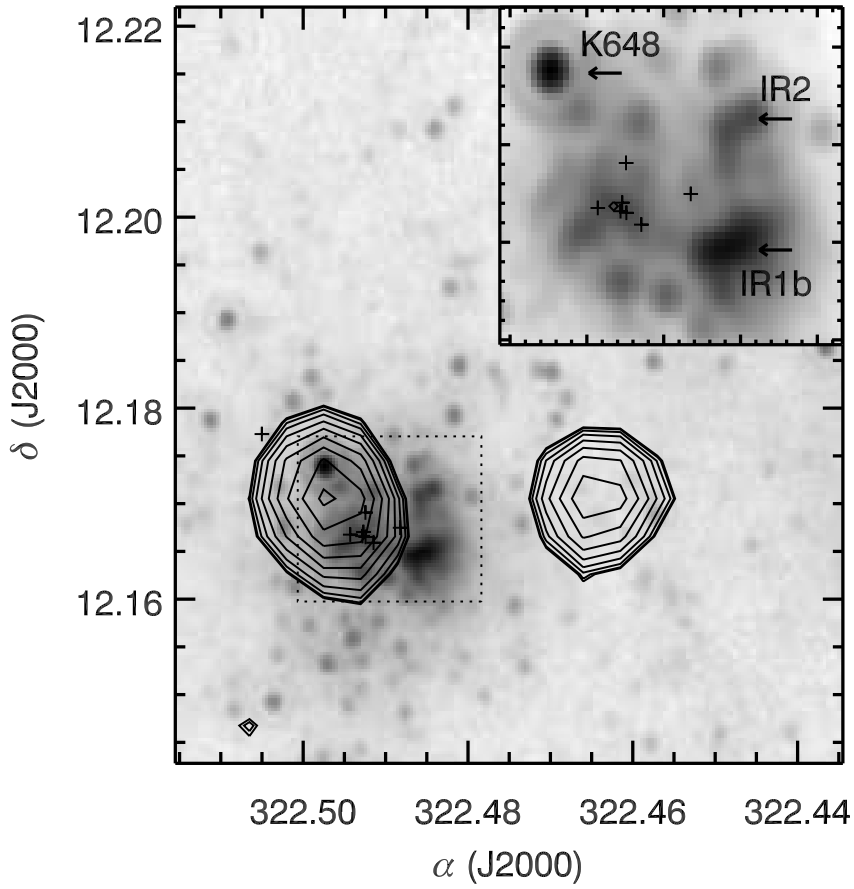

Fig. 10.— MIPS 24 μm mosaic overlayed with radio contours (1.4 GHz) (Condon et al. 1998). There are ten contour levels ranging from pixel values of 1.56 to 5.0 mJy/Beam on a square root scale. Pulsar locations are marked with an "+" symbol, and the center of the cluster is marked by a diamond. The inset (dotted lines) has dimensions of approximately $1.3' \times 1.0'$.

Table 1. M15 properties[a]

[Fe/H]	Core radius (")	Z-height (kpc)	τ_c (years)	$M_{cluster}$ ($M_\odot$)	V_{esc} (km s^{-1})	L ($L_\odot$)	E(B-V)	D (kpc)
-2.4	4.1	4.79	4x10^7	2x10^6	40.9	5.8x10^5	0.11	9.98±0.47

[a] Values reproduced from Evans et al. (2003), except E(B-V) from Schlegel et al. (1998) and distance from McNamara et al. (2004).

Table 2. Observational Summary

Instrument	AORkey	Exposure Time[a] (s)	Coverage	pixel size ("/pixel)
IRAC	12030208	10.4	9.5' x 9.5'	1.22
MIPS 24 μm	12030464	9.96	11' x 12'	1.245
MIPS 70 μm	12030464	10.49	8.5' x 14.5'	4.925
IRS	15733760	60 (SL)		

[a] Exposure time of individual BCD images. For IRAC, only medium exposure HDR frames are listed.

Table 3. Flux Densities[a] of Dusty IR Sources

ID[b]	r arcsec	3.6 μm	4.5 μm	5.8 μm mJy	8 μm	24 μm
2MASS J21295231+1210515	0.212	13.99±0.70	10.87±0.54	7.02±0.35	4.22±0.21	0.44±0.02
2MASS J21295264+1210440	0.201	6.24±0.31	10.21±0.51	8.64±0.43	5.09±0.25	0.66±0.02
SSTU J212953.55+120910.7	0.982	8.91±0.45	9.28±0.46	6.80±0.34	3.91±0.20	0.45±0.02
2MASS J21295383+1209338	0.200	6.15±0.31	1.43±0.07	5.22±0.26	5.00±0.25	0.61±0.02
2MASS J21295473+1208592	0.032	4.80±0.24	6.87±0.34	5.23±0.26	2.92±0.15	0.30±0.02
2MASS J21295618+1210179	0.030	21.08±1.05	24.61±1.23	22.05±1.10	>1.78±0.09	2.93±0.02
2MASS J21295678+1210269	0.271	30.65±1.53	30.35±1.52	>6.19±0.31	12.86±0.64	1.25±0.02
2MASS J21295703+1209376	0.242	4.79±0.24	23.99±1.20	17.84±0.89	9.78±0.49	-
2MASS J21295712+1210043	0.190	11.11±0.56	1.73±0.09	4.79±0.24	5.08±0.25	-
2MASS J21295716+1209175	0.250	17.59±0.88	15.18±0.76	12.41±0.62	3.56±0.18	0.67±0.02
2MASS J21295758+1209552	0.301	12.34±0.62	12.00±0.60	>0.27±0.01	3.45±0.17	-

Table 3—Continued

ID[b]	r arcsec	3.6 μm	4.5 μm	5.8 μm mJy	8 μm	24 μm
2MASS J21295756+1210276	0.022	6.06±0.30	-	>0.62±0.03	2.55±0.13	0.44±0.02
2MASS J21295815+1209466	0.493	18.20±0.91	28.30±1.41	21.12±1.06	8.83±0.44	1.66±0.02
2MASS J21295828+1209280	0.202	4.85±0.24	4.13±0.21	0.91±0.05	0.33±0.02	-
2MASS J21295832+1209128	0.181	8.03±0.40	7.32±0.37	5.40±0.27	4.98±0.25	0.50±0.02
2MASS J21295881+1209285	0.301	9.78±0.49	10.12±0.51	5.39±0.27	2.27±0.11	0.47±0.02
2MASS J21295937+1210029	0.420	8.35±0.42	7.35±0.37	8.61±0.43	1.06±0.05	-
SSTU J212959.69+120739.0[c]	4.722	0.31±0.04	0.29±0.02	0.26±0.02	1.47±0.07	2.37±0.02
2MASS J21295981+1211107	0.231	6.41±0.32	5.73±0.29	4.14±0.21	-	0.28±0.02
2MASS J21295996+1207282[d]	0.100	0.34±0.03	0.25±0.02	0.24±0.02	2.05±0.10	2.52±0.03
2MASS J21300062+1209284	0.140	2.95±0.15	4.05±0.20	>0.12±0.01	1.94±0.10	0.22±0.02
2MASS J21300097+1210375	0.054	5.78±0.29	6.11±0.31	4.41±0.22	2.50±0.12	0.31±0.02

Table 3—Continued

ID[b]	r arcsec	3.6 μm	4.5 μm	5.8 μm mJy	8 μm	24 μm
2MASS J21300277+1206557[e]	0.010	9.34±0.47	6.18±0.31	4.04±0.20	3.29±0.16	3.66±0.02

[a]Flux densities are color corrected and dereddened using E(B-V) = 0.11 and A_λ values from Indebetouw et al. (2005).

[b]Standard 2MASS designations are listed for all stars that have a 2MASS counterpart located within r = 0.5″ from the *Spitzer* coordinates. Otherwise, stars are listed with standard *Spitzer* designations where U stands for "unidentified".

[c]Designated as IR3a in text. 3.6, 4.5, and 5.8 μmfluxes were determined with aperture photometry in IDL, as this source was not detected by APEX at these wavelengths.

[d]Designated as IR3b in text. 3.6, 4.5, and 5.8 μmfluxes were determined with aperture photometry in IDL, as this source was not detected by APEX at these wavelengths.

[e]Designated as IR4 in text.

Table 4. ICM Dust (IR1a) Flux Densities

λ μm	F_λ[a] mJy	Instrument(s)/Mission(s)
0.56	4667.±233.	HST WFPC2[b]
1.25	10857.±186.	2MASS
1.65	10450.±204	2MASS
2.16	7342.±134.	2MASS
3.6	**3669.±1.**	**IRAC**
4.5	**2336.±1.**	**IRAC**
5.8	**1442.±1.**	**IRAC**
8.0	**757.7±0.5**	**IRAC**
24	**159.4±0.1**	**MIPS**
60	515.±155.	ISO[c]
70	**691.2±61.1**	**MIPS**
70	578.±173.	ISO[c]
90	303.±91.	ISO[c]

[a] Aperture size is 130.5 × 130.5 arcseconds, corresponding to the ISO aperture from Evans et al. (2003). All fluxes are dereddened with E(B-V)=0.11. A_λ values come from Rieke & Lebofsky (1985) and Indebetouw et al. (2005).

[b] From image U5B80101R from the public HST archives.

[c] From Evans et al. (2003).

Table 5. Spitzer Infrared Line Fluxes of K648

λ μm	Ion/Line	Flux[a] ergs cm^{-2} s^{-1}
12.81	[Ne II]	$(1.74 \pm 0.08) \times 10^{-13}$
12.35	H I $7-6$	$(9.75 \pm 3.08) \times 10^{-15}$
10.51	[S IV]	$(8.24 \pm 3.56) \times 10^{-15}$
7.46	H I $6-5$	$(4.38 \pm 0.68) \times 10^{-14}$

[a] Integrated line fluxes assuming a fixed IRS instrumental resolution of 0.0404 μm, and a Gaussian line profile.

Table 6. Sulfur and Neon Abundances for K648

Quanity	Value
T_e(K)	12,500
n_e(cm^{-3})	1,700
I([S II]6717,6731)/I(Hβ)[a]	$(1.69 \pm 1.12) \times 10^{-3}$
S^+/H^+	$(6.30 \pm 3.00) \times 10^{-9}$
I([S III]9532)/I(Hβ)[b]	$(7.59 \pm 3.37) \times 10^{-3}$
S^{2+}/H^+	$(2.55 \pm 1.13) \times 10^{-8}$
I([S IV]10.51 μm/I(Hβ)[c]	$(5.42 \pm 2.54) \times 10^{-3}$
S^{3+}/H^+	$(1.10 \pm 0.52) \times 10^{-8}$
Total S/H	$(4.28 \pm 1.28) \times 10^{-8}$
I([Ne III]3967)/I(Hβ)[d]	$(2.7 \pm 0.9) \times 10^{-3}$
Ne^{2+}/H^+	$(3.69 \pm 1.23) \times 10^{-6}$
I([Ne III]3969)/I(Hβ)[d]	$(1.19 \pm 0.30) \times 10^{-1}$
Ne^{2+}/H^+	$(4.89 \pm 1.23) \times 10^{-6}$
I([Ne II]12.81 μm/I(Hβ)[c]	$(1.15 \pm 0.18) \times 10^{-1}$
Ne^+/H^+	$(1.53 \pm 0.21) \times 10^{-5}$
Total Ne/H	$(2.39 \pm 0.27) \times 10^{-5}$
O/H[e]	$(5.0 \pm 1.3) \times 10^{-5}$
[S/O][f]	–2.64
[Ne/O] [f]	+0.54

[a] From Barker et al. (1983).

[b] From Barker et al. (1983). Note lines are blended.

[c] Hβ flux derived from *Spitzer* observations of H I recombination lines (see §3.2.1).

[d] From Adams et al. (1984). Measured values corrected for extinction (see §3.2.2).

[e] From Peña et al. (1993).

$$^{\mathrm{f}}[X] = log_{10}(X_{Object}) - log_{10}(X_{\odot}).$$

This figure "f1.png" is available in "png" format from:

http://arXiv.org/ps/astro-ph/0606236

This figure "f5.png" is available in "png" format from:

http://arXiv.org/ps/astro-ph/0606236

This figure "f7.png" is available in "png" format from:

http://arXiv.org/ps/astro-ph/0606236

This figure "f8.png" is available in "png" format from:

http://arXiv.org/ps/astro-ph/0606236